Proceedings of the 6th International Conference on Gas Hydrates (ICGH 2008),
Vancouver, British Columbia, CANADA, July 6-10, 2008.

PORE-SCALE MECHANISTIC STUDY OF THE PREFERENTIAL MODE OF HYDRATE FORMATION IN SEDIMENTS:

COUPLING OF MULTIPHASE FLUID FLOW AND SEDIMENT MECHANICS

Antone K. Jain, and Ruben Juanes*
Department of Civil and Environmental Engineering
Massachusetts Institute of Technology
77 Massachusetts Ave, Building 48-319, Cambridge MA 02139, USA

ABSTRACT

We present a discrete element model for the simulation, at the grain scale, of gas migration in brine-saturated deformable media. We account rigorously for the presence of two fluids in the pore space by incorporating grain forces due to pore fluid pressures, and surface tension between fluids. The coupled model permits investigating an essential process that takes place at the base of the hydrate stability zone: the upward migration of methane in its own free gas phase. We elucidate the way in which gas migration may take place: (1) by capillary invasion in a rigid-like medium; and (2) by initiation and propagation of a fracture. We find that the main factor controlling the mode of gas transport in the sediment is the grain size, and show that coarse-grain sediments favor capillary invasion, whereas fracturing dominates in fine-grain media. The results have important implications for understanding hydrates in natural systems. Our results predict that, in fine sediments, hydrate will likely form in veins that follow a fracture-network pattern, and the hydrate concentration in this type of accumulations will likely be quite low. In coarse sediments, the buoyant methane gas is likely to invade the pore space more uniformly, in a process akin to invasion percolation, and the overall pore occupancy is likely to be much higher than for a fracture-dominated regime. These implications are consistent with field observations of methane hydrates in natural systems.

Keywords: gas hydrates, porous media, natural systems, multiphase flow, fracturing, capillary pressure, discrete element model (DEM)

NOMENCLATURE

A_j	effective area of pore throat j [m^2]
b	Biot coefficient [-]
c_v	coefficient of consolidation [Pa]
C_j	conductance of pore throat j [m^4/Pa/s]
$\tilde{C}_j$	dimensionless conductance of pore throat j [-]
d	gap at grain–grain "contact" [m]
$\boldsymbol{F}$	force vector [N]
F^n	normal contact force [N]
F^s	tangential contact force [N]
$\mathbf{I}_i$	tensor of moments of inertia of grain i [N.m]
k	intrinsic permeability [m^2]
k_n	normal contact stiffness [N/m]
k_s	shear contact stiffness [N/m]
K_f	bulk modulus of the fluid [Pa]
K_s	bulk modulus of the solid grain [Pa]
L_j	effective length of pore throat j [m]
$\boldsymbol{M}$	moment vector [N.m]
m_i	mass of particle i [kg]
p	fluid pressure [Pa]
p_D	dimensionless fluid pressure [-]
p_g	gas pressure [Pa]
p_w	water pressure [Pa]
P_c	capillary pressure [Pa]
Q_D	dimensionless fluid flow rate [-]
q_j	fluid flow rate through pore throat j [m^3/s]
r_g	grain radius [m]
$r_{\min}$	minimum grain radius of assembly [m]
δt	time step [s]
U_n	grain overlap [m]
ΔU_s	tangential displacement [m]
V_p	volume of a pore [m^3]
$w(=1)$	width of 2D assembly in third dimension [m]
$\boldsymbol{x}_i$	position vector of grain i centroid [m]

*Corresponding author. Phone: +1 617 253 7191; Fax: +1 617 258 8850; Email: juanes@mit.edu

Greek letters

γ	interfacial tension [N/m]
$\boldsymbol{\theta}_i$	angle vector of rotation of grain i [-]
μ	fluid viscosity [Pa.s]
$\bar{\mu}$	contact friction coefficient [-]
ξ	dimensionless distance [-]
ρ_s	grain density [kg/m^3]
σ	total stress [Pa]
σ'	effective stress [Pa]
σ_H	horizontal Earth stress [Pa]
σ_V	vertical Earth stress [Pa]
$\bar{\sigma}_c$	normal contact strength in stress units [Pa]
$\bar{\tau}_c$	shear contact strength in stress units [Pa]
τ	dimensionless time [-]
φ_n	normal contact strength in force units [N]
φ_s	shear contact strength in force units [N]

INTRODUCTION

Methane hydrates are crystalline ice-like compounds, composed of methane molecules caged in a lattice of water molecules [1]. Hydrates form naturally at high pressures and low temperatures, like those typical of most of the ocean floor. It is believed that an enormous pool of carbon exists in the form of methane gas and methane hydrate in the ocean floor along the continental margins. Some estimates of the size of this reservoir suggest that the amount of energy is of the order of all other fossil fuels combined, although these estimates are highly uncertain [2]. It also seems likely that this pool of carbon plays an important role in the global carbon cycle [3], and in massive submarine landslides [4].

Methane hydrate systems in ocean sediments have been the subject of intense research in recent years. A significant component of that effort is directed towards gaining a better conceptual picture of the hydrogeological environment of gas hydrate systems. Particular attention has been devoted to the two end-members [5]:

1. The hydrogeologically more active, dynamic end-member, exemplified by Hydrate Ridge, offshore Oregon [6–10].

2. The hydrogeologically less active, quiescent end-member, illustrated by Blake Ridge, offshore South Carolina [11, 12].

One of the fundamental observations at these two sites is the co-existence of methane hydrate, gas and brine within the HSZ. This is especially noticeable in dynamic environments [13, 14], but has been observed in low-flux hydrate provinces [15]. There is by now conclusive evidence that methane transport through the HSZ cannot occur solely as dissolved methane in the aqueous phase. The scientific community is now undergoing a heated debate as to what are the reasons for co-existence [16–18], which include: (1) kinetics of hydrate formation; (2) regional geotherms; (3) hypersaline brines as a result of hydrate formation; and (4) fast, focused flow of free gas through fractures and high-permeability conduits. The importance of methane migration as a separate gas phase, and the need to account for multiphase flow effects coupled with hydrate formation, have already been pointed out a decade ago [19, 20].

It has been proposed that free gas accumulation beneath the HSZ may reach a critical thickness to open fractures in the sediment or activate pre-existing faults that will serve as conduits for fast upwards gas migration [21–25]. In this case, it is clear that the study of the hydrate system must be coupled with the mechanical response of the host sediments containing hydrate.

Our research is aimed at testing the following hypothesis [26, 27]: the coupling between drainage and fracturing, both induced by pore pressure, determines whether methane gas entering the hydrate stability zone (HSZ) is converted completely to hydrate. In a companion paper [28], a novel implementation of the level set method (LSM) is used to determine the capillarity-controlled displacement of brine by gas from sediment and from fractures within the sediment.

In this paper, we present a discrete element method (DEM) to model the strong coupling that takes place between the pore fluids and the mechanical behavior of the sediment. We account rigorously for the presence of one or more fluids in the pore space by incorporating additional sets of forces due to pore fluid pressures and interfacial tension between the fluids. We demonstrate the ability of DEM to reproduce core-scale behavior, as measured by triaxial laboratory experiments and fluid flow tests. The proposed methodology elucidates the depositional environments (grain size, earth stresses, and sediment cohesion) under which migration of methane gas by fracturing of the sediment is favored over capillary invasion. This determines the distribution of methane gas and hydrate which, in turn, has direct implications on the likelihood that gas and hydrate will co-exist, and on the overall size of the energy resource.

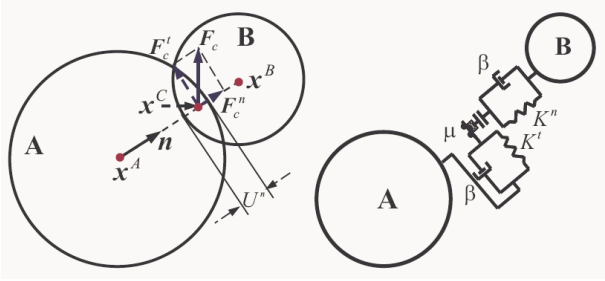

Figure 1: Schematic diagram of a grain–grain contact (left) and the associated contact model in a Discrete Element Model (right) [32].

THEORY, FORMULATION AND METHODS

The Discrete Element Method (DEM) [29] has proved a valuable tool to study the mechanisms for deformation and failure of granular materials with variable degree of cementation [30]. Moreover, based on simple geometric arguments, stress variations (and subsequent deformation) have been shown to affect flow properties such as porosity and permeability [31].

Each element or grain is identified separately by its own mass, moment of inertia and contact properties. For each grain, its translational and rotational movements are described by solving Newton's second law of motion. The mechanical behavior at the deformation region of grain contact is approximated by introducing a grain contact model, such as a system of a spring, dashpot and slider (Figure 1).

Discrete Element Modeling of "dry" media

The movement of a grain is dictated by the net force and moment acting on it. For a *dry model*, that is, one in which pore pressures are negligible, the forces for each grain may include: (1) contact force $\boldsymbol{F}_c$ due to the deformation at the grain contacts, (2) damping forces $\boldsymbol{F}_d$ due to grain non-elastic collisions; (3) external forces $\boldsymbol{F}_b$ due to gravity and prescribed tractions at the boundaries. The contact force $\boldsymbol{F}_c$ can be further split into normal and tangential components, $\boldsymbol{F}_c^n$ and $\boldsymbol{F}_c^s$, respectively.

The simplest (linear elastic) mechanical behavior at the grain contacts is described by the following equations:

$$F^n = k_n U_n, \quad \Delta F^s = -k_s \Delta U_s, \tag{1}$$

where U_n is the overlap, ΔU_s is the tangential displacement, and k_n and k_s are the normal and shear stiffness at the contact, respectively [33, 34]. Inelastic behavior emerges due to either slip between grains, or breakage of contact bonds. Inelasticity is reflected by the constraints:

$$F^s \leq \bar{\mu} F^n, \quad F^n \leq \varphi_n, \quad F^s \leq \varphi_s, \tag{2}$$

where $\bar{\mu}$ is the contact friction coefficient, and φ_n and φ_s are the normal and shear strengths (in force units) of the contact.

Bulk behavior of a granular system is determined by all individual grain–grain interactions. For the analysis of dry samples, the interactions between particles can be associated with a network of grain–grain contact forces that connects the centroids of grains that are in contact.

Given the set of forces $\boldsymbol{F}_j$ and moments $\boldsymbol{M}_j$ acting on the ith particle, its motion is described by the following equations:

$$m_i \ddot{\boldsymbol{x}}_i = \sum_j \boldsymbol{F}_j, \tag{3}$$

$$\mathbf{I}_i \ddot{\boldsymbol{\theta}}_i = \sum_j \boldsymbol{M}_j. \tag{4}$$

Here, $\boldsymbol{x}_i$ and $\boldsymbol{\theta}_i$ are the position vector of the grain centroid and the angle vector of rotation about the centroid; the double dots denote second time derivatives of the position and rotation angle; m_i is the mass; and $\mathbf{I}_i$ is the tensor of moments of inertia, respectively. The equations of motion (3)–(4) must be solved simultaneously for all grains in the system via a numerical integration scheme. In DEM, explicit solution schemes with a single force evaluation per time step are preferred. A commercial three-dimensional DEM code, PFC2D [34], was used.

Micromechanical vs. macroscopic parameters. The parameters that need to be defined at the grain-scale level are ρ_s, $\bar{\mu}$, k_n, k_s, φ_n and φ_s, as well as the grain size distribution, which we shall characterize simply by the radius interval $[r_{\text{min}}, r_{\text{max}}]$.

From DEM simulations of biaxial tests, the linear elastic *macroscopic* parameters (Young modulus E and Poisson ratio ν), as well as strength properties (yield stress σ_y, friction angle φ, cohesion c, etc.) may be computed. In order to obtain macroscopic parameters that are independent (or only slightly dependent) on the grain size, the contact strengths must scale with the grain size [33]:

$$\varphi_n = \bar{\sigma}_c 2 r_g w, \quad \varphi_s = \bar{\tau}_c 2 r_g w, \tag{5}$$

where $\bar{\sigma}_c$ and $\bar{\tau}_c$ are the normal and shear contact strengths (in stress units)—assumed to be independent of grain size— and w is the width of the 2D assembly in the third dimension.

Time step selection for mechanics simulation. Since explicit time integration is used, the time step is bounded by stability considerations. The characteristic time required to capture the dynamics is [34]

$$\delta t \sim \sqrt{m_i/k_i}. \tag{6}$$

In PFC2D, grains are assumed to by disks of unit width ($w = 1$ m), so $m = 2\pi r_g^2 w \rho_s$ and, therefore, the critical time step for mechanical stability scales as follows:

$$\delta t_{\text{crit}}^{\text{m}} \sim \sqrt{\rho_s/k_n} r_g, \tag{7}$$

where ρ_s is the grain density, k_n is the grain normal stiffness, and r_g is the grain radius.

Micro-poromechanics of single-fluid systems

From the theory of poromechanics [35], it is well known that pore pressure will influence mechanical behavior. Essentially, compressive stresses in granular media are transmitted both through a solid skeleton and the pore fluids. Recently, models have been developed to incorporate this effect in DEM with a single-phase pore fluid [36–39].

When the pore space is filled with a single fluid phase at non-negligible pressure, the associated forces must be incorporated in the model. A conceptual view of the new set of forces is shown in Figure 2. Computationally, the model then consists of two overlapping and interacting networks: the grain network and the fluid network. A particular instance is shown in Figure 3. The force that the fluid in one of the domains exerts on a particular grain is obtained by integrating the pressure along the contact area. In our implementation, a pressure force is directed from the midpoint of the segment joining grain contacts to the grain center. Therefore, pressure forces do not induce rotation.

Consider one particular fluid domain, as sketched in Figure 4. The micromechanical equations can be summarized as follows. The flow rate out of the fluid domain through a pore throat is

$$q_j = C_j \frac{p - p_j}{L_j}, \tag{8}$$

where C_j is the throat conductance and L_j is an effective distance between pore centers. The conductance is inversely proportional to the fluid viscosity μ, and proportional to the square of the effective throat area A_j:

$$C_j = \frac{\tilde{C}_j}{\mu} \frac{A_j^2}{2r_g} w, \tag{9}$$

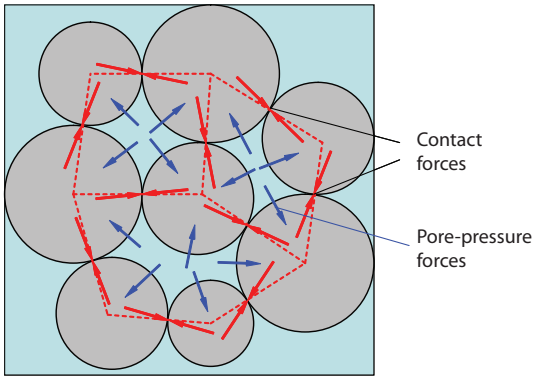

Figure 2: Conceptual picture of the fluid-solid interaction model at the pore scale when a single fluid is present.

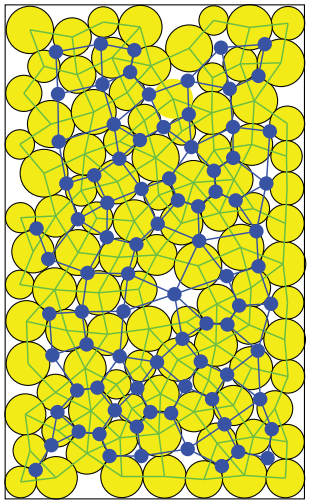

Figure 3: Representation of the grain assembly (yellow circles) and the network (green lines). At the center of each fluid domain is a pore body (blue dots).

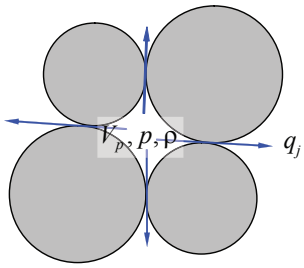

Figure 4: Schematic representation of a fluid domain. At any given time, each fluid domain is characterized by its pore volume V_p, and the pressure p and density ρ of the fluid. Fluid can go in and out of the pore domain at a rate q_j into the neighboring fluid domains.

where $\tilde{C}_j$ is a dimensionless throat conductance. The derivation of this equation from the solution of a Stokes flow problem, and the expressions for $\tilde{C}$ and A, are given in [40].

The grains have certain compressibility, and the radius of a spherical grain varies according to

$$r_g = r_{g,0}\left(1 - \frac{p}{3K_s}\right), \tag{10}$$

where $r_{g,0}$ is the initial radius (at zero fluid pressure), K_s is the bulk modulus of the solid grain, and p is the average of the pressure around the grain. Finally, mass balance over a fluid domain gives the following pressure evolution equation for a pore volume:

$$\delta p = \frac{K_f}{V_p}\left(-\delta V_p - \sum_j q_j \delta t\right), \tag{11}$$

where K_f is the fluid bulk modulus, and δp is the pressure variation after a time step δt. The main feature of our model is the term $-\delta V_p$, which accounts for the change in volume of each pore caused by changes in grain locations. This term has been neglected in previous investigations of pore-scale poromechanical models but is essential, for example, to reproduce pressurization of the fluid upon fast compaction. It also reflects the reverse coupling present in Biot's self-consistent theory of poroelasticity.

There is a formal analogy between the micro-poromechanical equations presented above, and Biot's self-consistent theory of poroelasticity [35, 41]. We expect that the DEM formulation will reproduce the linear theory of poroelasticity only in the range of small deformations and small pressure changes. Under such conditions, the poroelastic parameters can then be determined from DEM simulations. When these conditions are not met, nonlinear/irreversible behavior is expected to emerge in the DEM model, driven by contact slip, bond breaking and grain rearrangement.

Time step selection for fluid flow simulation. The grain-scale fluid flow equations (11) are solved using an explicit time integration scheme. The time step must be restricted for the scheme to be stable. The characteristic time associated with the microscopic fluid flow dynamics is

$$\delta t \sim \frac{V_p}{K_f}\frac{\delta p}{\sum_j q_j}. \tag{12}$$

Introducing Equations (8) and (9), we express the characteristic time as

$$\delta t \sim \frac{V_p}{K_f}\frac{2r_g\mu}{w}\sum_j \frac{L_j}{\tilde{C}_j A_j^2}. \tag{13}$$

Using the scaling $V_p \sim r_g^2 w$, and $A \sim r_g^2$, the critical time step for fluid flow stability scales as follows:

$$\delta t^{\mathrm{f}}_{\mathrm{crit}} \sim \frac{\mu}{\tilde{C}K_f}. \tag{14}$$

In a coupled poromechanics simulation, the time step must be smaller than the minimum of the critical values in Equations (7) and (14).

Micro-poromechanics of two-fluid systems

In the environments of interest for methane hydrates—in particular, at the base of the hydrate stability zone—two fluid phases exist: a liquid brine phase, and methane gas. One of the key differences between single-fluid and two-fluid systems is the presence of a fluid–fluid interface. Due to surface tension effects, the pressures on both sides of the interface (that is, the pressure of brine and the pressure of methane gas) can be very different.

The key question is: what is the preferential mode of gas invasion? Two different fundamental mechanisms are at play (Figure 5): (1) capillary-dominated invasion of a rigid solid skeleton, and (2) fracturing of the sediment. While capillarity governs invasion of gas through the porous medium, mechanical effects may lead to deformation and fracturing of the sediment skeleton, thereby triggering invasion when it would otherwise not occur. Preferential fracturing of the sediment requires differences in pressure between neighboring pores. While this is typically not a favored scenario in single-fluid systems (unless a fluid is injected at very fast flow rates and pressures, as in hydraulic fracturing operations), it is natural in two-fluid systems because the two fluids have different pressures. Since the two fluids do not mix, a pressure difference does not dissipate. This pressure difference may lead to preferential fracturing of the sediment. Methane invasion by fracture opening is common, as evidenced by field observations of tensile fractures at the seafloor and hydrate layers along bedding planes [6]. These processes clearly couple flow and deformation, at both the grain scale and the macroscopic scale.

Here, we adopt an "elastic membrane" representation of the gas/water interface that only allows normal forces to be transmitted (Figure 6). Consider

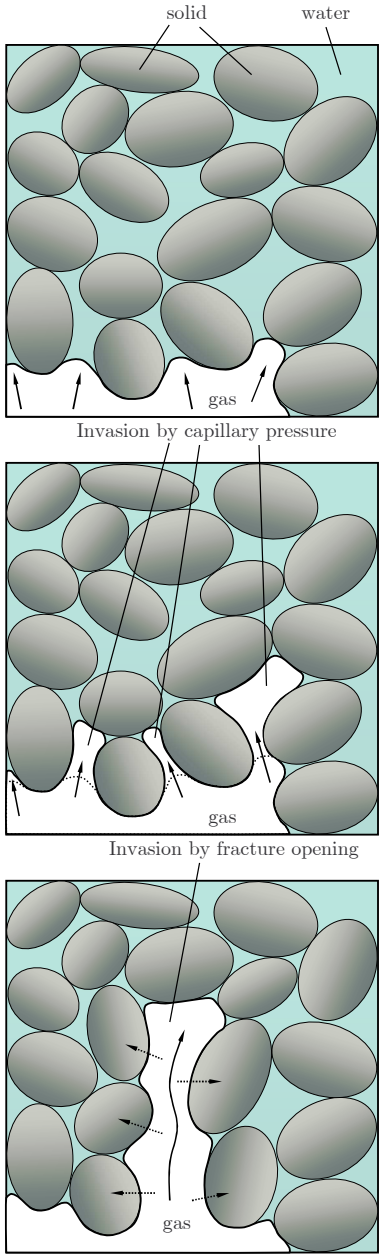

Figure 5: Schematic diagram of the two modes of methane gas invading a sediment. **Top:** before invasion, the gas–water interface of a buoyant gas plume underlies water-filled sediment. **Middle:** invasion will occur if the capillary pressure (the difference between gas pressure and water pressure) exceeds the capillary entry pressure, which is inversely proportional to the pore diameter. **Bottom:** invasion by fracture opening; if the exerted pressure is sufficient to overcome compression and friction at grain contacts, a fracture will form. In a multiphase environment, due to surface tension effects, the gas pressure will *not* dissipate quickly through the porous medium, and water at grain contacts will increase cohesion.

invasion of methane free gas by capillary invasion (Fig. 5(middle)). The gas/water interface will invade a throat if the capillary pressure (that is, the difference between gas pressure and water pressure) is larger than the capillary entry pressure [42–44]. The capillary entry pressure is proportional to the interfacial tension γ, and inversely proportional to the throat opening. Let d be the throat gap (which, in a 2D model, may be negative if there is overlap between the grains). In [40], we derive the following expression for the gas pressure to invade a throat:

$$p_g - p_w \geq \frac{2}{\sqrt{1 + \left(1 + \frac{d}{2r}\right)^2} - 1} \frac{\gamma}{r_g}. \qquad (15)$$

Clearly, if the grain size is large, this process is favored and gas invasion can occur even if the porous medium is rigid. On the other hand, for small grain size (high capillary entry pressures), gas invasion will not occur until the grains are pushed apart (Fig. 5(bottom)). For cohesionless material, this will occur when the gas pressure exceeds the minimum compressive stress:

$$p_g \geq \sigma_H. \qquad (16)$$

In [40], we extend this condition of fracture opening to the case when cohesion $\bar{\sigma}_c$ exists (either by cementation, consolidation, or capillary adhesion). The fracturing pressure depends not only on the Earth stresses and the cohesive stress, but also on the length of a pre-existing fracture and, importantly, on the grain size. This last dependency emanates from the observation that the internal lengthscale in the fracture toughness is determined by the grain size [33]. In any case, it is the nonlinear evolution of the DEM micro-poromechanical model that determines when bonds break, and when the gap between grains is large enough for the gas interface to advance, according to Equation (15). In this fashion, the "membrane" advances and a new pore is loaded with a higher pressure.

The implementation of multi-fluid poromechanics is therefore very similar to that of single-fluid systems, except that the key hydraulic property (the conductance between pore bodies) is set to zero until condition (15) is satisfied.

While capillary invasion and fracture opening are the two end-member mechanisms for methane transport in its own gas phase, our coupled grain-scale model allows us to investigate the competition between the two as a function of grain size, Earth stresses, and sediment cohesion.

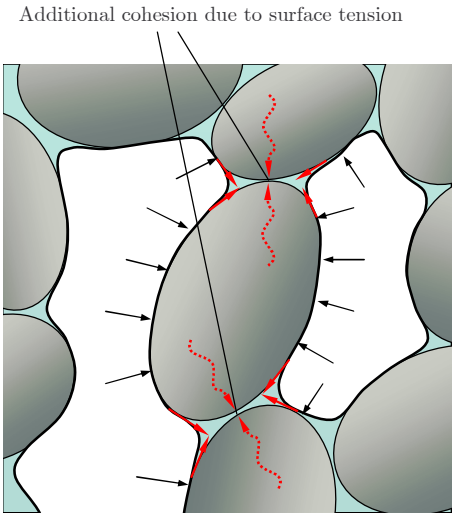

Figure 6: Meniscus pinning in the presence of two fluid phases in the sediment. During multiphase flow in porous media, the least wetting phase (gas) migrates through the center of the pores, while the most wetting phase (brine) coats the grains and forms filaments around the crevices of the pore space. This configuration leads to gas–water menisci around the grain contacts. Due to interfacial tension, these menisci are responsible for an attraction force between grains. At the macroscopic level, this can be interpreted as an increment in the cohesion of the material. This is a purely multiphase-flow effect, not present in single-phase poromechanics.

RESULTS

Sediment model generation and initialization

A model sediment is generated by first choosing the number of particles, and reproducing the desired grain size distribution. As we shall see below, several macroscopic properties (both mechanical and fluid-flow properties) are dependent on the grain size. Therefore, it is important that the sediment model either reproduces the desired grain size distribution, or that the assigned microproperties (e.g. bond strength) reflect the disparity in grain size [33]. In most of the examples shown in this paper, we have chosen a relatively narrow, uniform distribution $[r_{\min}, r_{\max}]$, with $r_{\max} = (5/3)r_{\min}$.

The particles are randomly placed in a box and allowed to fall under gravity, simulating sedimentation (Figure 7). The settling process has two differentiating stages: (1) free fall under gravity, with limited grain–grain interaction, and (2) settling and grain rearrangement until static conditions are reached.

In Figure 8 we show the evolution of the time step

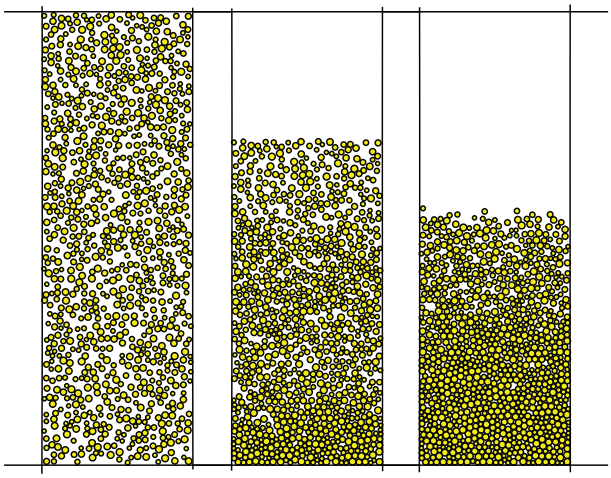

Figure 7: Snapshots of the particle settling process.

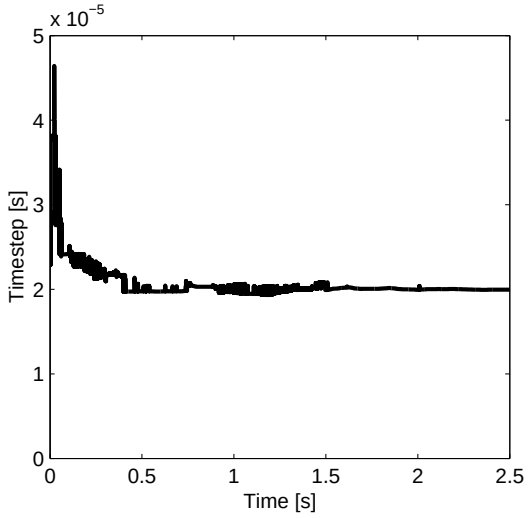

Figure 8: Evolution of the time step during the settling process.

during the settling process. The time step is larger initially, during the "free fall" stage, and quickly converges to the value required for stability of the dynamical system dominated by grain–grain interactions. The scaling of the time step with grain radius and grain stiffness is shown in Figure 9, confirming the stability condition of Equation (7): the time step is proportional to the grain radius, and inversely proportional to the square root of the grain stiffness.

Uniaxial compaction for "dry" media

Here we show that DEM simulations of "dry" media (infinitely compressible pore fluid) are able to capture the mechanical behavior of real sediments. In Figure 10 we plot experimental stress–strain curves

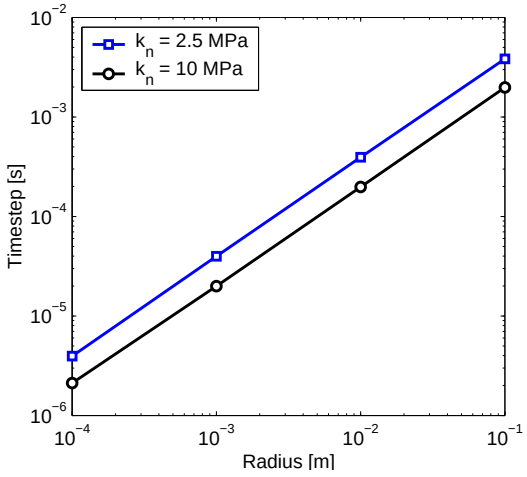

Figure 9: Scaling of the time step with grain radius.

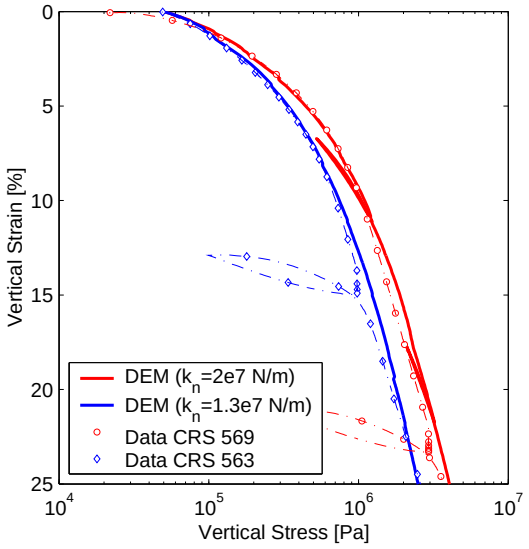

Figure 10: Experimental stress–strain curves for sediments from Hydrate Ridge [45], and comparison with DEM simulations for two different values of the grain stiffness.

of sediment samples from Hydrate Ridge [45] along with curves from DEM simulations. The DEM model sediments reproduce approximately the grain size distribution of actual sediments, and the only parameter that we varied to reproduce measured stress–strain behavior was the grain stiffness k_n. The rest of the micromechanical parameters are as follows: $k_s = k_n$, $\bar{\mu} = 0.5$, $\bar{\sigma}_c = \bar{\tau}_c = 0$.

The DEM simulations match the stress–strain behavior measured in the lab even for very high deformations (up to 25% strain), capturing the material nonlinearity. The DEM model also displays irreversible behavior in that loading/unloading cycles show hysteresis. However, it is unable to reflect the dramatic reduction in stiffness upon unloading that the data show.

Uniaxial fluid flow

In this section, we evaluate the fluid flow capabilities of the grain-scale model. We do so by simulating a one-dimensional fluid flow problem in a cell with drained top and bottom boundaries, and impervious fixed lateral boundaries. The initial pressure is constant, and equal to the boundary pressures. Suddenly, a pressure change is applied to the top boundary, and we simulate the evolution of the pressure and fluid inflow/outflow until a new steady state is reached. The problem is described mathematically by the partial differential equation:

$$c_v \frac{\partial p}{\partial t} - \frac{k}{\mu}\frac{\partial^2 p}{\partial x^2} = 0, \quad 0 < x < H, \tag{17}$$

where k is the intrinsic permeability, μ is the fluid viscosity, and c_v is the consolidation coefficient [41]. The initial condition is given by:

$$p(x,0) = 0, \quad 0 \le x \le H, \tag{18}$$

and the boundary conditions are:

$$p(0,t) = 0, \quad p(H,t) = \Delta p, \quad t > 0. \tag{19}$$

The problem can be expressed in dimensionless form by defining the following dimensionless quantities:

$$\text{distance: } \xi = \frac{x}{L},$$

$$\text{time: } \tau = \frac{t}{T_c}, \quad T_c = \frac{c_v \mu H^2}{k},$$

$$\text{pressure: } p_D = \frac{p}{\Delta p},$$

$$\text{flow rate: } Q_D = \frac{Q}{Q_c}, \quad Q_c = \frac{k}{\mu}\frac{\Delta p}{H} W w,$$

where W is the width and w is the thickness of the cell (that is, the dimensions of the cell in the directions perpendicular to the flow). The analytical solution to the problem can be found by the method of separation of variables. The dimensionless pressure field is given by:

$$p_D(\xi,\tau) = \xi + \frac{2}{\pi}\sum_{n=1}^{\infty}\frac{(-1)^n}{n}\sin(n\pi\xi)\exp(-(n\pi)^2\tau). \tag{20}$$

By differentiating the expression above, we find the expression for the dimensionless flow rate in and out of the cell:

$$Q_D^{\text{in}} = 1 + 2\sum_{n=1}^{\infty}(-1)^n \cos(n\pi)\exp(-(n\pi)^2\tau), \tag{21}$$

$$Q_D^{\text{out}} = 1 + 2\sum_{n=1}^{\infty}(-1)^n \exp(-(n\pi)^2\tau). \tag{22}$$

The objective is to determine whether the grain-scale model reproduces the macroscopic behavior. The relevant macroscopic parameters are the intrinsic permeability k and the consolidation coefficient c_v. The intrinsic permeability is obtained by matching the flow rate at steady state. The consolidation coefficient is determined by matching the dimensionless inflow and outflow curves.

We generated an assembly with 1000 grains, and a minimum radius $r_{\text{min}} = 1$ cm. The vertical and horizontal dimensions of the cell are, approximately, $H = 1$ m and $W = 0.7$ m. We set the pressure increment Δp to a small value, so that the effects of pore pressure on the mechanical deformation are minimal. Once the flow stabilizes, inflow and outflow rates are equal to Q_c, and the intrinsic permeability of the medium can be computed as:

$$k = \frac{\mu H Q_c}{W w \Delta p}. \tag{23}$$

The characteristic time T_c is then obtained by matching the numerical inflow and outflow curves, from which the macroscopic consolidation coefficient is computed as:

$$c_v = \frac{kT_c}{\mu H^2}. \tag{24}$$

In Figure 11 we plot the dimensionless inflow and outflow rates as a function of dimensionless time. The agreement between the DEM results and the analytical solution is remarkable, indicating that the flow formulation accurately captures the macroscopic behavior (Darcy flow in porous media). As a further validation of the model, we compare in Figure 12 the evolution of dimensionless pore pressure within the sample. By plotting the pressure values from the DEM simulation at individual pores, we obtain a scattered profile of the average pressure as a function of depth. We compare these results with the analytical solution at different dimensionless times. Again, the agreement is remarkable.

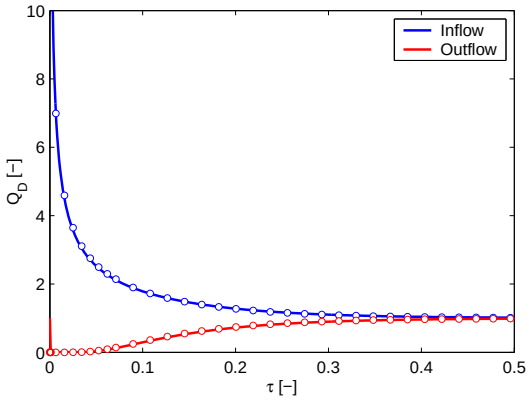

Figure 11: Inflow and outflow rates into the pressure cell. Comparison of DEM simulation (dotted line) and analytical solution (solid line).

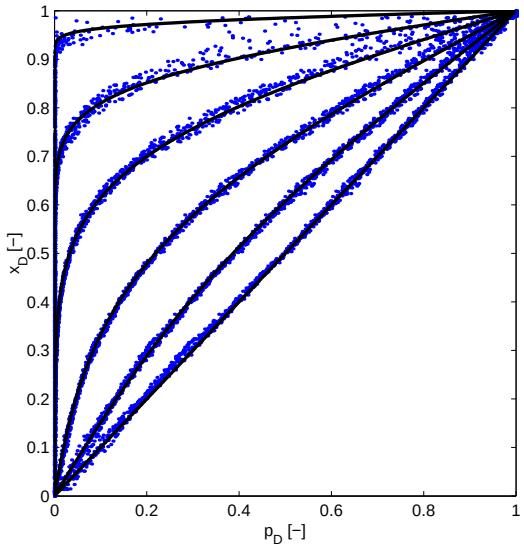

Figure 12: Evolution of pressure profiles during the uniaxial fluid flow test. Comparison of DEM simulation (dotted line) and analytical solution (solid line) at different dimensionless times: $\tau = 0.000242$, 0.00671, 0.0275, 0.0829, 0.175, 1.404.

Table 1: Macroscopic hydraulic and poromechanical parameters for different grain size distributions.

r_{min} [m]	k [m^2]	c_v/K_f [-]
0.01	0.289×10^{-6}	0.161
0.001	0.289×10^{-8}	0.156

By repeating the fluid flow simulations with different values of $r_{\min}$, we determine the dependence of the hydraulic and poromechanical parameters on grain size. The results are compiled in Table 1, where we confirm that the intrinsic permeability scales with the square of the grain size (as expected from Stokes theory, and the Kozeny–Carman relation for granular materials). Moreover, if the fluid is significantly more compressible that the skeleton, the DEM simulations also reflect that the effective consolidation coefficient c_v is inversely proportional to K_f, with the constant of proportionality being approximately equal to the porosity [41].

Uniaxial undrained compaction

A sensitive test towards validation of the DEM coupled model is fluid–solid behavior during undrained consolidation tests. A sediment model is initialized by gravitational settling. Then the walls are adjusted to achieve an isotropic confining stress state of 0.1 MPa. Until that point, the fluid is allowed to drain and the pressure is atmospheric ($p = 0$ MPa). After that, the sample is sealed so that no fluid is allowed to drain, and it is subjected to uniaxial compaction. During the undrained compaction process, the vertical strain ε, total vertical stress σ, and average pore pressure p are recorded. In view of the effective stress concept [35, 46], the total stress required to achieve a given deformation in a fluid-saturated medium is larger than for a dry medium. In the realm of the linear theory of poroelasticity, the *effective stress* is given by:

$$\sigma' = \sigma - bp, \tag{25}$$

where b is the Biot coefficient. The dependence of the Biot coefficient on the solid and fluid properties of the constituents is reasonably well understood [41, 47]. The Biot coefficient approaches a value of one only in the limit of incompressible grains. If the grain and fluid compressibilities are comparable, the Biot coefficient is less than one.

We used an assembly with 100 grains, $r_{\min} = 0.01$ m, $k_n = 10^7$ N/m, $k_n/k_s = 2.5$, and $K_f = 10^7$ Pa. In Figure 13 we show the stress–strain curves for a cemented/cohesive sample (bond strength $\bar{\sigma}_c = \bar{\tau}_c = 10^6$ Pa—left figure), and for an unconsolidated/cohesionless sample (bond strength $\bar{\sigma}_c = \bar{\tau}_c = 10^2$ Pa—right figure). In both cases, we plot the stress–strain curves for the fluid-saturated medium (total stress), and for a dry medium. We confirm that the dry stress curve can

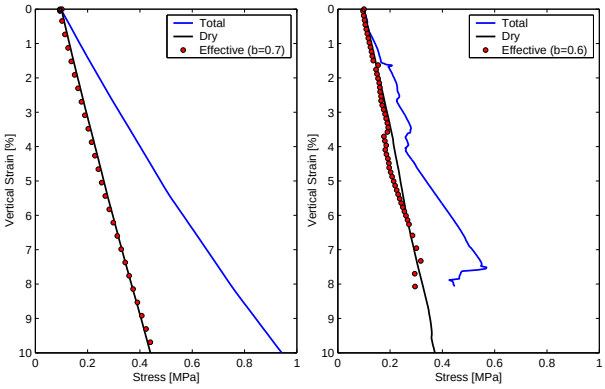

Figure 13: Stress–strain curves for uniaxial undrained compaction. Left: cemented/cohesive sample. Right: unconsolidated/cohesionless sample.

be interpreted as the effective stress, and recovered by subtracting the pore pressure times the Biot coefficient from the total stress. In this way, the Biot coefficient can be inferred. Figure 13 illustrates the proper behavior of the coupled DEM model in two ways: (1) the results are in agreement with the Biot theory of poroelasticity (at least in the region of small strains); and (2) the values of b inferred from the simulation also agree well with experimental values [41, Table C.1].

Fracturing vs. capillary invasion

Migration of a gas phase through a deformable medium may occur by two end-member mechanisms: (1) capillary invasion through a rigid medium, and (2) fracture opening. Our DEM model is capable of reproducing *both* mechanisms, and therefore predict the conditions under which one is favored over the other, and gas migration as a result of their *combined* effect.

Capturing the fracturing phenomenon. We first illustrate that our DEM model of coupled two-phase fluid flow and grain mechanics can reproduce fracture initiation and propagation, upon invasion of an immiscible gas phase. As explained earlier, we adopt an "elastic membrane" representation of the gas/water interface that only allows normal forces to be transmitted. The formulation of adhesion forces due to surface tension effects [48] is greatly simplified at this stage. If the gas cannot invade a throat by capillarity, the gas pressure will act to separate the grains. When the bond between two grains is lost, and the gap between them increases sufficiently, the

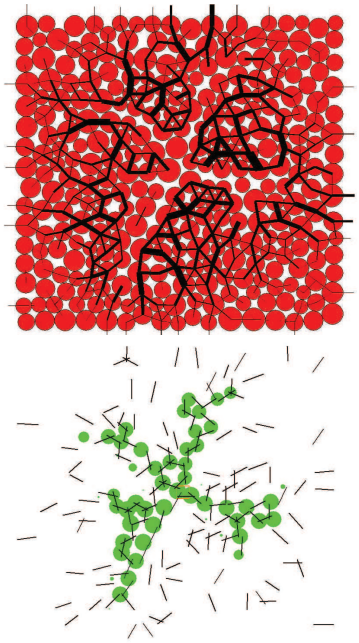

Figure 14: Illustration of the fracturing behavior of a model sediment upon injection of gas, when the vertical and horizontal stresses are equal. The sediment fractures "isotropically" into a set of radial, geometrically-complex fractures.

"membrane" advances and a new pore is loaded with a higher pressure.

Influence of Earth stresses. In many (passive) depositional environments, the horizontal stress is lower than the vertical stress. In such scenarios, one expects the development of vertical fractures that open up the sediment in the direction of minimum compressive stress.

In Figure 14 we show that fracturing of the sediment is not necessarily restricted to anisotropic Earth stresses. Even when horizontal and vertical stresses are equal, the medium tends to fracture in a set of radial, geometrically complex fractures, if gas is injected into a brine-saturated sediment.

Influence of grain size. We find that the most sensitive factor in determining the mode of methane gas transport (sediment fracturing or capillary invasion) is the grain size: fracturing is favored for fine-grained sediments, while capillary invasion is favored for coarse-grained sediments. We will report on our theoretical analysis of this competition, as well as on the quantitative validation of the coupled grain-scale model, in future communications. Here we simply illustrate the two end-member systems.

The simulation is set up as follows. A sample of 300 grains of grain size $[r_{\min}, 2r_{\min}]$ is generated by gravitational settling. The sediment is compacted under constant pore pressure until a desired stress state is achieved. We impose an anisotropic stress state, with effective stresses $\sigma'_V = 10$ kPa, and $\sigma'_H \approx 8$ kPa. The interfacial tension is $\gamma = 50 \times 10^{-3}$ N/m. We assume that the cohesion is inversely proportional to grain radius. This is phenomenologically adequate (fine-grained material like clays are cohesive) and is also consistent with the adhesive forces that result from the presence of a gas–water interface [49]. For simplicity, we take $\bar{\sigma}_c = 10\gamma/r_g$. The only parameter that is left free is the grain size $r_{\min}$.

In Figure 15 we show two snapshots of the evolution of the methane–water interface for a coarse-grain sediment of characteristic size $r_{\min} = 1$ mm. It is apparent that during the invasion of methane gas, there is virtually no movement of the solid grains: the sediment acts like a rigid skeleton. Indeed, the network of grain contact compressive forces remains the same during the process. Invasion of gas from pore to pore occurs when the gas pressure (minus the water pressure) exceeds the capillary entry pressure of the throat (Equation (15)). In this case, the capillary entry pressure is much lower than the fracturing pressure (the left figure corresponds to $P_c \approx 0.17$ kPa), and fluid transport is well described by *invasion percolation* [50, 51]. Ultimately, if the gas pressure is sufficiently high, almost all the pores have been invaded by methane gas. In this case, this occurs at a slightly higher capillary entry pressure of $P_c \approx 0.2$ kPa.

The behavior is completely different when a much smaller grain size is used. The evolution of the methane gas migration for $r_{\min} = 1$ μm is shown in Figure 16. The range of capillary entry pressure for the initial configuration is now in the order of 150 kPa. However, at this pressure, mechanical effects are become dominant, and the solid skeleton no longer behaves like a rigid medium. At around $P_c \approx 150$ kPa, the invading gas starts to initiate a fracture, with its characteristic stress concentration at the fracture tip captured by the DEM model [33] (left plot). At a slightly higher pressure ($P_c \approx 160$ kPa), the fracture propagates vertically. The case presented here is interesting in that it displays *some* competition between fracture opening and capillary invasion—note the invaded pores

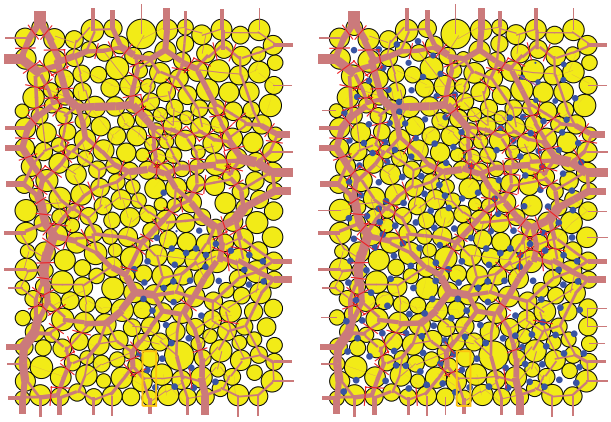

Figure 15: Snapshots of the evolution of the methane gas–water interface for the case $r_{\min} = 1$ mm. The pores occupied by gas are represented with blue dots. The brown lines indicate compression at grain–grain contacts. Left: $P_c \approx 0.17$ kPa. Right: $P_c \approx 0.20$ kPa.

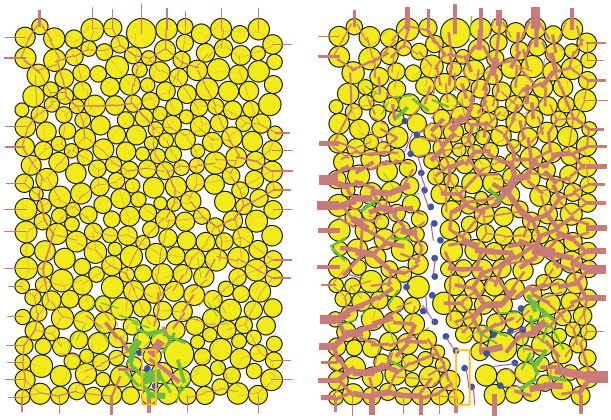

Figure 16: Snapshots of the evolution of the methane gas–water interface for the case $r_{\min} = 1$ μm. The pores occupied by gas are represented with blue dots. The brown lines indicate compression at grain–grain contacts. The green lines represent tension, which is supported by cohesion between grains. Left: $P_c \approx 150$ kPa. Right: $P_c \approx 160$ kPa.

to the right of the fracture. Fracture opening, however, dominates the vertical migration of methane in its free gas form.

DISCUSSION AND CONCLUSIONS

We have presented a discrete element model for the simulation, at the grain scale, of gas migration in brine-saturated deformable media. The model has been validated for many processes, including: (1) generation of sediment models by gravitational settling and compaction; (2) stress–strain behavior of ocean sediments; (3) transient single-phase flow for determination of hydraulic parameters; (4) undrained compaction tests for determination of poromechanical parameters.

The coupled model permits investigating an essential process that takes place at the base of the hydrate stability zone: the upward migration of methane in its own free gas phase. We elucidate the way in which gas migration may take place: (1) by capillary invasion in a rigid-like medium; and (2) by initiation and propagation of a fracture.

Each end member can be analyzed separately, and conditions for gas invasion can be found the capillary-dominated and fracture-dominated regimes. The significant contribution of our coupled model is that it captures both phenomena and, as a result, allows us to study the transition between the two regimes. We find that the main factor controlling the mode of gas transport in the sediment is the grain size. We have shown that coarse-grain sediments favor capillary invasion, whereas fracturing dominates in fine-grain media.

These emergent phenomena have important implications for understanding hydrates in natural systems (either ocean sediments and permafrost regions). Our model predicts that, in fine sediments, hydrate will likely form in veins that follow a fracture-network pattern. Since the mechanism of fracture propagation is self-reinforcing, our results indicate that it is possible, and even likely, that methane gas will penetrate deeply into the HSZ (and maybe all the way to the ground surface). The hydrate concentration in this type of accumulations will likely be quite low.

Our model supports the view that, in coarse sediments, the buoyant methane gas is likely to invade the pore space more uniformly, in a process akin to invasion percolation. While this is definitely affected by heterogeneity in grain-size distribution, the overall pore occupancy is likely to be much higher than for a fracture-dominated regime.

The predictions from our model are entirely consistent with field observations of hydrates in natural systems [6, 21–25].

ACKNOWLEDGMENTS

We thank Carolyn Ruppel for interesting discussions, and John T. Germaine for providing the laboratory data in Figure 10. This work was supported by the Department of Energy under Grant DOE/NETL DE-FC26-06NT43067. This support is gratefully acknowledged.

REFERENCES

[1] E. D. Sloan. *Clathrate Hydrates of Natural Gases*. Marcel Deker, New York, second edition, 1998.

[2] E. D. Sloan. Fundamental principles and applications of natural gas hydrates. *Nature*, 426:353–359, November 23, 2003.

[3] G. R. Dickens. Rethinking the global carbon cycle with a large, dynamic and microbially mediated gas hydrate capacitor. *Earth Planet. Sci. Lett.*, 213:169–183, 2003.

[4] C. K. Paull, P. G. Brewer, W. Ussler, E. T. Peltzer, G. Rehder, and D. Clague. An experiment demonstrating that marine slumping is a mechanism to transfer methane from seafloor gas-hydrate deposits into the upper ocean and atmosphere. *Geo-Mar. Lett.*, 22:198–203, 2003.

[5] A. M. Trehu, C. Ruppel, M. Holland, G. R. Dickens, M. E. Torres, T. S. Collett, D. Goldberg, R. Riedel, and P. Schultheiss. Gas hydrates in marine sediments: lessons from scientific drilling. *Oceanography*, 19(4):124–143, 2006.

[6] E. Suess, M. E. Torres, G. Bohrmann, R. W. Collier, J. Greiner, P. Linke, G. Rehder, A. Trehu, K. Wallman, G. Winckler, and E. Zuleger. Gas hydrate destabilization: enhanced dewatering, benthic material turnover and large methane plumes at the Cascadia convergent margin. *Earth Planet. Sci. Lett.*, 170:1–15, 1999.

[7] M. D. Tryon, K. M. Brown, and M. E. Torres. Fluid and chemical flux in and out of sediments hosting methane hydrate deposits on Hydrate Ridge, OR, II: Hydrological processes. *Earth Planet. Sci. Lett.*, 201:541–557, 2002.

[8] A. M. Trehu, P. E. Long, M. E. Torres, G. Bohrmann, F. R. Rack, T. S. Collett, D. S. Goldberg, A. V. Milkov, M. Riedel, P. Schultheiss, N. L. Bangs, S. R. Barr, W. S. Borowski, G. E. Claypool, M. E. Delwiche, G. R. Dickens, E. Gracia, G. Guerin, M. Holland, J. E. Johnson, Y. J. Lee, C. S. Liu, X. Su, B. Teichert, H. Tomaru, M. Vanneste, M. Watanabe, and J. L. Weinberger. Three-dimensional distribution of gas hydrate beneath southern Hydrate Ridge: constraints from ODP Leg 204. *Earth Planet. Sci. Lett.*, 222:845–862, 2004.

[9] J. L. Weinberger, K. M. Brown, and P. E. Long. Painting a picture of gas hydrate distribution with thermal images. *Geophys. Res. Lett.*, 32:L04609, doi:10.1029/2004GL021437, 2005.

[10] K. U. Heeschen, A. M. Trehu, R. W. Collier, E. Suess, and G. Rehder. Distribution and height of methane bubble plumes on the Cascadia Margin characterized by acoustic imaging. *Geophys. Res. Lett.*, 30(12):Art. No. 1643, doi:10.1029/2003GL016974, 2003.

[11] W. S. Holbrook, H. Hoskins, W. T. Wood, R. A. Stephen, and D. Lizarralde. Methane hydrate and free gas on the Blake Ridge from vertical seismic profiling. *Science*, 273:1840–1842, September 27, 1996.

[12] G. R. Dickens, C. K. Paull, and P. Wallace. Direct measurement of in situ methane quantities in a large gas-hydrate reservoir. *Nature*, 385:426–428, 1997.

[13] A. V. Milkov, G. R. Dickens, G. E. Claypool, Y.-J. Lee, W. S. Borowski, M. E. Torres, W. Xu, H. Tomaru, A. M. Trehu, and P. Schultheiss. Co-existence of gas hydrate, free gas, and brine within the regional gas hydrate stability zone at Hydrate Ridge (Oregon margin): evidence from prolongued degassing of a pressurized core. *Earth Planet. Sci. Lett.*, 222:829–843, 2004.

[14] M. E. Torres, K. Wallman, A. M. Trehu, G. Bohrmann, W. S. Borowski, and H. Tomaru. Gas hydrate growth, methane transport, and chloride enrichment at the southern summit of Hydrate Ridge, Cascadia margin off Oregon. *Earth Planet. Sci. Lett.*, 226:225–241, 2004.

[15] A. R. Gorman, W. S. Holbrook, M. J. Hornbach, K. L. Hackwith, D. Lizarralde, and I. Pecher. Migration of methane gas through the hydrate stability zone in a low-flux hydrate province. *Geology*, 30 (4):327–330, 2002.

[16] A. V. Milkov and W. Xu. Comment on "Gas hydrate growth, methane transport, and chloride enrichment at the southern summit of Hydrate Ridge, Cascadia margin off Oregon" by Torres et al. [Earth Planet. Sci. Lett. 226:225–241 (2004)]. *Earth Planet. Sci. Lett.*, 239:162–167, 2005.

[17] M. E. Torres, K. Wallman, A. M. Trehu, G. Bohrmann, W. S. Borowski, and H. Tomaru. Reply to comment on: "Gas hydrate growth, methane transport, and chloride enrichment at the southern summit of Hydrate Ridge, Cascadia margin off Oregon". *Earth Planet. Sci. Lett.*, 239:168–175, 2005.

[18] C. Ruppel, G. R. Dickens, D. G. Castellini, W. Gilhooly, and D. Lizarralde. Heat and salt inhibition of gas hydrate formation in the northern Gulf of Mexico. *Geophys. Res. Lett.*, 32:L04605, doi:10.1029/2004GL021909, 2005.

[19] G. D. Ginsburg and V. A. Soloviev. Methane migration within the submarine gas-hydrate stability zone under deep-water conditions. *Mar. Geol.*, 137: 49–57, 1997.

[20] V. A. Soloviev and G. D. Ginsburg. Water segregation in the course of gas hydrate formation and accumulation in submarine gas-seepage fields. *Mar. Geol.*, 137:59–68, 1997.

[21] P. B. Flemings, X. Liu, and W. J. Winters. Critical pressure and multiphase flow in Blake Ridge gas hydrates. *Geology*, 31(12):1057–1060, 2003.

[22] A. M. Trehu, P. B. Flemings, N. L. Bangs, J. Chevalier, E. Gracia, J. E. Johnson, C.-S. Liu, X. Liu, M. Riedel, and M. E. Torres. Feeding methane vents and gas hydrate deposits at south Hydrate Ridge. *Geophys. Res. Lett.*, 31:L23310, doi:10.1029/2004GL021286, 2004.

[23] X. Liu and P. B. Flemmings. Passing gas through the hydrate stability zone at southern Hydrate Ridge, offshore Oregon. *Earth Planet. Sci. Lett.*, 241:211–216, 2006.

[24] M. J. Hornbach, D. M. Saffer, and W. S. Holbrook. Critically pressured free-gas reservoirs below gas-hydrate provinces. *Nature*, 427(6970):142–144, 2004.

[25] J. L. Weinberger and K. M. Brown. Fracture networks and hydrate distribution at Hydrate Ridge, Oregon. *Earth Planet. Sci. Lett.*, 245:123–136, 2006.

[26] R. Juanes and S. L. Bryant. Mechanisms leading to co-existence of methane gas and hydrate in ocean sediments. Technology status assessment report, U.S. Department of Energy, DOE/NETL Grant DE-FC26-06NT43067, November 2006.

[27] J. Behseresht, Y. Peng, M. Prodanovic, S. L. Bryant, A. K. Jain, and R. Juanes. Mechanisms by which methane gas and methane hydrate coexist in ocean sediments. In *Offshore Technology Conference*, Houston, TX, May 5–8, 2008. (OTC 19332).

[28] J. Behseresht, Y. Peng, M. Prodanovic, and S. L. Bryant. Pore-scale mechanistic study of the preferential mode of hydrate formation in sediments: Role of capillarity. In *Proc. 6th Intl. Conf. Gas Hydrates (ICGH 2008)*, Vancouver, Canada, July 6–10, 2008.

[29] P. A. Cundall and O. D. L. Strack. Discrete numerical model for granular assemblies. *Geotechnique*, 29:47–65, 1979.

[30] M. S. Bruno and R. B. Nelson. Microstructural analysis of the inelastic behavior of sedimentary rock. *Mech. Mater.*, 12(2):95–118, 1991.

[31] M. S. Bruno. Micromechanics of stress-induced permeability anisotropy and damage in sedimentary rocks. *Mech. Mater.*, 18:31–48, 1994.

[32] G. Jin. *Physics-Based Modeling of Sedimentary Rock Formation and Prediction of Transport Properties*. PhD Dissertation, University of California at Berkeley, Spring 2006.

[33] D. O. Potyondy and P. A. Cundall. A bonded-particle model for rock. *Int. J. Rock Mech. Min. Sci.*, 41:1329–1364, 2004.

[34] ITASCA. *PFC2D, v3.1 – Theory and Background*. Itasca Consulting Group, Inc., Minneapolis, MN, 2004.

[35] M. A. Biot. General theory of three-dimensional consolidation. *J. Appl. Phys.*, 12(155–164), 1941.

[36] Y. Shimizu. Fluid coupling in PFC2D and PFC3D. In Y. Shimizu, R. D. Hart, and P. Cundall, editors, *Numerical Modeling in Micromechanics Via Particle Methods. Proc. of the 2nd International PFC Symposium, Kyoto, Japan*, pages 281–287, Balkema, Leiden, October 2004.

[37] B. K. Cook, D. R. Noble, and J. R. Williams. A direct simulation method for particle-fluid systems. *Eng. Comput.*, 21(2–4):151–168, 2004.

[38] L. Li and R. M. Holt. Simulation of flow in sandstone with fluid coupled particle model. In *Rock Mechanics in the National Interest. Proceedings of the 38th U.S. Rock Mechanics Symposium, Washington, D.C.*, volume 1, pages 165–172, Balkema, Rotterdam, July 2001.

[39] L. Li and R. M. Holt. A study on the calculation of particle volumetric deformation in a fluid coupled PFC model. In Y. Shimizu, R. D. Hart, and P. Cundall, editors, *Numerical Modeling in Micromechanics Via Particle Methods. Proc. of the 2nd International PFC Symposium, Kyoto, Japan*, pages 273–279, Balkema, Leiden, October 2004.

[40] R. Juanes and S. L. Bryant. Mechanisms leading to co-existence of methane gas and hydrate in ocean sediments. Task 4: Fracture initiation and propagation, U.S. Department of Energy, DOE/NETL Grant DE-FC26-06NT43067, May 2008.

[41] H. F. Wang. *Theory of Linear Poroelasticity*. Princeton University Press, 2000.

[42] L. A. Richards. Capillary conduction of liquids through porous mediums. *Physics*, 1:318–333, 1931.

[43] M. C. Leverett. Capillary behavior of porous solids. *Petrol. Trans.* AIME, 142:152–169, 1941.

[44] R. P. Mayer and R. A. Stowe. Mercury porosimetry-breakthrough pressure for penetration between packed spheres. *J. Colloid Interface Sci.*, 20:893, 1965.

[45] B. B. Tan et al. Data report: Consolidation and strength characteristics of sediments from ODP Site 1244, Hydrate Ridge, Cascadia continental margin. In *Proc. Ocean Drilling Program, Sci. Results*, volume 204, 2006.

[46] K. Terzaghi. *Theoretical Soil Mechanics*. John Wiley, New York, 1943.

[47] O. Coussy. *Mechanics of Porous Media*. John Wiley & Sons, Chichester, England, 1995. Originally published in French as *Mécanique des Milieux Poreux*, Editions Technip, 1991.

[48] F. M. Orr, L. E. Scriven, and A. P. Rivas. Pendular rings between solids: meniscus properties and capillary force. *J. Fluid Mech.*, 67:723–742, 1975.

[49] S. Kato, T. Sakakibara, and H. Yoshimori. Effects of intergranular adhesive force on behavior of granular material. In Y. Shimizu, R. D. Hart, and P. Cundall, editors, *Numerical Modeling in Micromechanics Via Particle Methods. Proc. of the 2nd International PFC Symposium, Kyoto, Japan*, pages 347–354, Balkema, Leiden, October 2004.

[50] R. Lenormand, E. Touboul, and C. Zarcone. Numerical models and experiments on immiscible displacements in porous media. *J. Fluid Mech.*, 189: 165–187, 1988.

[51] D. Wilkinson and J. Willemsen. Invasion percolation: a new form of percolation theory. *J. Phys. A*, 16:3365–3376, 1983.